Supplementary Information for

Synchrotron X-ray quantitative evaluation of transient deformation and damage phenomena in a single Nickel-rich cathode particle

León Romano Brandt[a,*], John-Joseph Marie[b], Thomas Moxham[a], Dominic P. Förstermann[b], Enrico Salvati[a], Cyril Besnard[a], Chrysanthi Papadaki[a], Zifan Wang[a] , Peter G. Bruce[b,c,d,e] and Alexander M. Korsunsky[a]

[a]Korsunsky group, Multi-Beam Laboratory for Engineering Microscopy (MBLEM), Department of Engineering Science, University of Oxford, Parks Road, Oxford OX1 3PJ, United Kingdom

b Department of Materials, University of Oxford, Parks Road, Oxford, OX1 3PH, United Kingdom

c Department of Chemistry, University of Oxford, South Parks Road, Oxford OX1 3QZ, United Kingdom

d The Henry Royce Institute, Parks Road, Oxford, OX1 3PH, United Kingdom

e The Faraday Institution, Quad One, Becquerel Avenue, Harwell Campus, Didcot, OX11 0RA, United Kingdom

$LiNi_{0.8}Mn_{0.1}Co_{0.1}O_2$ cathode material in powder form as well as on 18mm electrode coins was purchased from Custom Cells Itzehoe GmbH.

T-EBSD Analysis

T-EBSD analysis was carried out on a thin, electron transparent lamella extracted from a cracked particle charged to 100% SoC at a rate of C/3, following one formation cycle at a rate of C/10. Kikuchi patterns were collected in transmission geometry at an angle of 45 degrees and their grain orientation indexed using NMC811 unit cell information implemented for this purpose based on literature data [1], as shown in Figure 1. A Tescan LYRA3 instrument was used for the t-EBSD acquisition at a beam energy of 20 keV and a pixel size of 40x40 nm^2. The obtained Euler angles in the sample x-y geometry were converted to *c*-axis vectors, based on which the angle α between the radial particle direction from the particle centre to the t-EBSD measurement location and the local *c*-axis was determined, as illustrated in Figure 1. Higher statistical occurrences of angles around 90 degrees were accounted for by normalising the angle distribution curve by $1/(0.5\sin(\alpha))$.

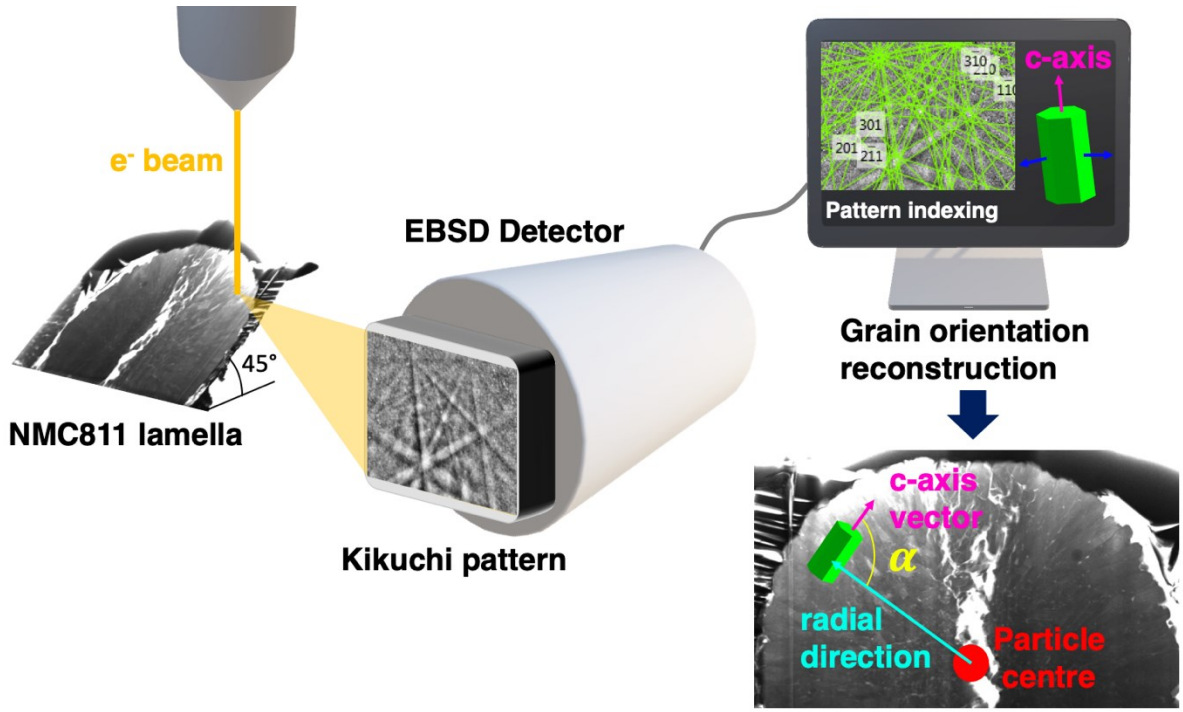

Figure 1. Illustration of the t-EBSD acquisition process (left) with subsequent pattern indexing and grain orientation reconstruction (right). Bottom right: illustration of the angle α between radial direction and *c*-axis vector used for determining the lithium diffusion direction

Operando Single Particle Diffraction

A custom synchrotron beamline setup, as illustrated in Figure 2, was built for the B16 beamline at Diamond Light Source, permitting a single NMC811 particle to be charged in Argon atmosphere, while acquiring diffraction patterns. Samples were prepared by sputter-coating industrial standard nano-manipulator needles with Aluminium, in order to prevent any tungsten oxidation during particle charge. One single particle per needle was attached inside the vacuum chamber of a Tescan LYRA3 XM FIB-SEM instrument using a platinum gas injection system. The samples were stored in a mobile vacuum container with desiccant pad at low vacuum. To mount the sample, it was removed from the container and held underneath a constant stream of argon, before being lowered into the Kapton container filled with Argon. The same procedure was followed for lithium disc, which were individually stored in a sealed vacuum containers until the experiment. A LiTFSI:PYR13 ionic liquid droplet was deposited onto the Li disc in Argon environment through a syringe, avoiding exposure to air. The particle was charged using a BioLogic SP-300 potentiostat in 30 pA constant-current mode, starting from a

voltage of 3.0V at a C-rate of 0.025 for a total duration of 15500s. An upper voltage limit of 4.5V was set as termination condition, however, due to increased internal resistance and resulting overpotential caused by the use of low vapour pressure ionic liquid, charging stopped prematurely at a SoC of 10.3%.

The SoC was determined post-experimentally by estimating the volume of the particle based on SEM images, yielding a particle volume of $2.13 \cdot 10^{-15}$ m^3. Assuming a density of $\rho_{NMC811} = 2200\ kg/m^3$ [2], the total particle mass was estimated to be $4.69 \cdot 10^{-12}$ kg. Assuming a specific capacity of 275.5 mAh/g provided by the powder supplier, combined with the transferred capacity at the end of charge of 28.3 mAh/g, this results in a final SoC of 10.3%.

KB mirrors were used to focus the 19 keV beam to a vertical and horizontal full width at half maximum of 380 nm and 800 nm, respectively. The vertical scanning path ranged from the lower end of the Al-coated tungsten needle to the lower free edge of the attached particle. Diffraction patterns for 003 and 104 reflections were acquired for 20s using a Photonic Science Image Star 9000 detector with a resolution of 3056x3056 pixels and individual pixel size of 31x31 μm^2. A sample-detector distance of 131.67 mm was determined using LaB_6 powder diffraction calibration. Image files were calibrated, integrated and reduced using the DAWN Science software package [3] and finally converted to d-spacing using MATLAB.

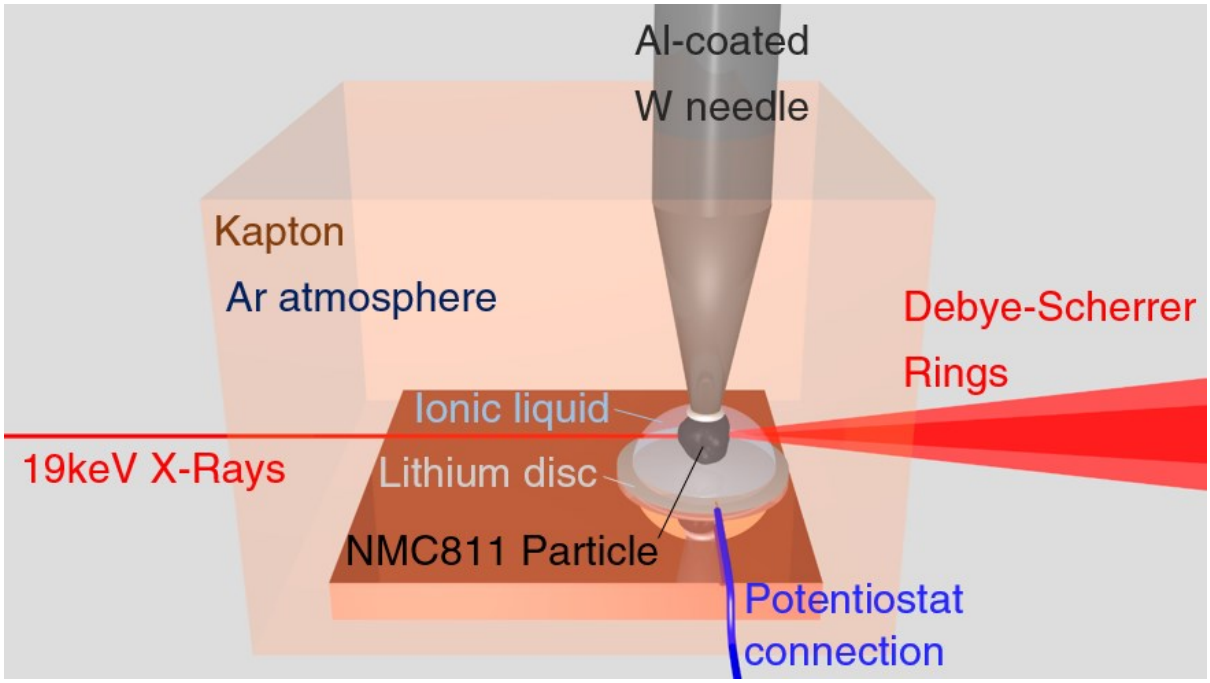

Figure 2. Operando synchrotron setup permitting to charge a single particle operando, while acquiring diffraction patterns and ensuring inert gas atmosphere

Full cell operando diffraction

In a second experiment at Diamond Lightsource Beamline B16, a custom cell design was used for *operando* XRD measurements at an X-Ray energy of 19 keV and a beam size of 10.1x2 mm^2. Carbon windows on either side of the cell allowed X-rays to pass through with little attenuation, while also doubling as current collectors. Measurements were carried out in transmission mode. The cell was made into a half cell configuration with NMC 811 being measured vs a Li metal anode. 1M LiPF6 in EC:DMC (50:50) was used as the electrolyte system. The cell was charged from 3.4 to 4.4V at a rate of 0.5C. Following the identical calibration and integration procedure as described for the single particle measurements, the c-axis and a-axis lattice parameter evolution were reconstructed using MATLAB. The results of the average cathode lattice parameter evolution versus SoC are shown in Figure 3.

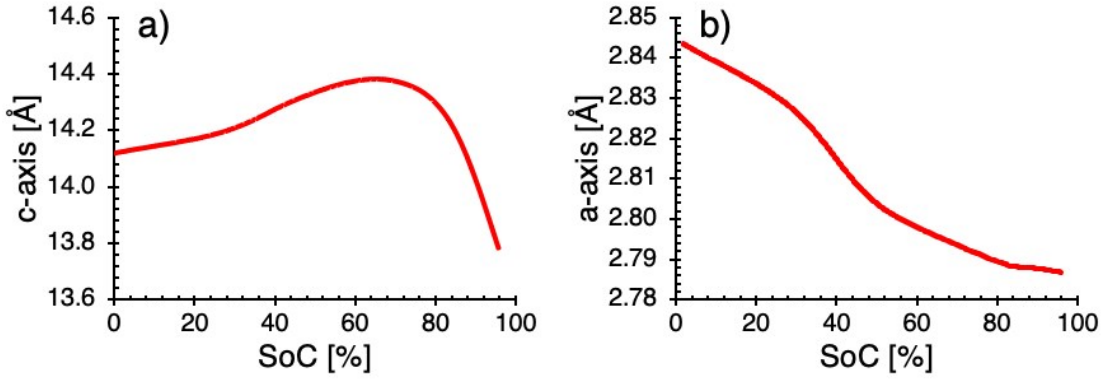

Figure 3. Lattice parameter evolution during full cell charge of NMC811 at a rate of 0.5C. (a) C-axis lattice parameter. (b) A-axis lattice parameter.

In situ Ptychography and Reconstruction

Ptychographic imaging was carried out on the I13-1 beamline (coherence branch) at Diamond Light Source, U.K. A similar sample setup as for the *operando* particle diffraction was built for the experiment. The particle was charged at a C-rate of 0.205 up to an SoC of 17.8% for a total duration of 3100s. As for the diffraction experiment, the voltage reading was not reliable

due to overpotential induced by the use of ionic liquid. A particle mass of $5.23 \cdot 10^{-9}$ g was determined by multiplying the reconstructed tomography volume with a density of $\rho_{NMC811} = 2200\ kg/m^3$. Assuming a specific capacity of 275.5 mAh/g provided by the powder supplier, combined with the transferred capacity at the end of charge of 49.0 mAh/g, this results in a final SoC of 17.8%.

A Fresnel zone plate with beam stop and order sorting aperture were used to focus coherent X-rays at an energy of 9.7 keV onto the sample which was place slightly downstream of the focus. Diffraction patterns were collected in the far-field 9.47m from the sample using an Excalibur detector, which features an array of Medipix3 chips and has a $55\mu m$ x $55\mu m$ pixel size. For each angular projection 256 diffraction patterns were generated by raster scanning with an aperiodic $1\mu m$ step over an area of 16 x 16 μm^2. Ptychography scans were repeated for 600 evenly spaced angular positions of the sample rotated though 180°.

The diffraction data was cropped to 512 x 512 pixels around the optical axis in order to include only statistically significant counts. Ptychographic reconstructions were performed using 500 iterations of the ePIE algorithm [4] which resulted in a sample pixel size of around $43nm$ x 43 nm. Prior to tomographic reconstruction the sample phase was unwrapped and had a phase ramp subtracted. Alignment of the projection stack was based on the sequential re-projection algorithm with the tomography reconstructions carried out using the standard filtered back-projection algorithm.

Modelling and Simulation

A simplified model of a secondary particle was realised by creating a 90° circle sector and applying appropriate symmetry conditions, resulting in a 2D particle slice under plane strain approximation. The particle radius *R* was chosen to be 10µm, while the values for density ($\rho_{NMC811} = 2200\ kgm^{-3}$ [2]), Young's modulus ($E = 170\ GPa$ [5]) and Poisson ratio ($\nu = 0.25$ [6]) were obtained from literature. The diffusion coefficient of Li in NMC 811 was adopted from literature ($D_{Li} = 10^{-10}\ cm^2 s^{-1}$ [7,8]) and assumed constant. Subsequently, diffusion and expasion dicrections for both random particle orientation and core-shell type particles were prescribed. Core-shell type particles were modelled by prescribing homogenous diffusion (blue area in Figure 5a) and expansion (blue area in Figure 5b) properties in the core of the particle, thus

approximating a secondary particle core composed of small primary particles with random crystal orientations. The nanorod shell was modelled to permit diffusion exclusively in radial direction (red area in Figure 5a) and expansion only in hoop direction (red area in Figure 5b). This radial diffusion behaviour was mathematically expressed by the diffusion coefficient of a core-shell particle c_{CS}:

$$c_{CS} = \begin{pmatrix} Dx & 0 \\ 0 & Dy \end{pmatrix} = D_{Li}\begin{pmatrix} \mathrm{H}' + \cos\left(\arctan2\left(y,x\right)\right) \cdot H & 0 \\ 0 & H' + \sin\left(\arctan2\left(y,x\right)\right) \cdot H \end{pmatrix}. \quad (1)$$

$H' = f(x,y,w,R_T,R)$ and $H = f(x,y,w,R_T,R)$ are two smooth Heaviside functions, which describe the transition from homogenous to radial diffusion properties and are depending on the location x, y, as well as the transition radius R_T and the transition width w. H' dominates the diffusion behaviour up to R_T for the particle core, after which the diffusion for the shell is described by H. Figure 4 shows an example of the horizontal diffusion coefficient component *Dx,* along with all parameters used to define the Heaviside function. The transition width w was chosen to be 0.1µm, as the core-shell particles usually exhibit a rather abrupt change in morphology between core and shell.

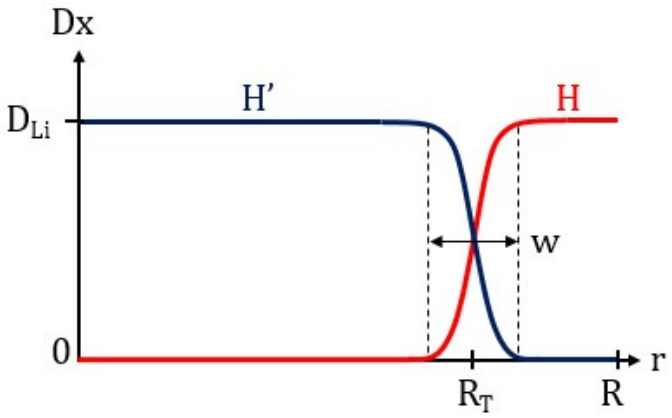

Figure 4. Example of the diffusion coefficient definition for the horizontal diffusion coefficient component Dx in horizontal direction for a core-shell particle.

The randomly oriented particle, in contrast, was assumed to permit homogenous diffusion and expansion across the entire particle (Figure 5c). The diffusion coefficient for a random particle c_R was therefore defined as:

$$c_R = \begin{pmatrix} Dx & 0 \\ 0 & Dy \end{pmatrix} = D_{Li}\begin{pmatrix} 1 & 0 \\ 0 & 1 \end{pmatrix}. \quad (2)$$

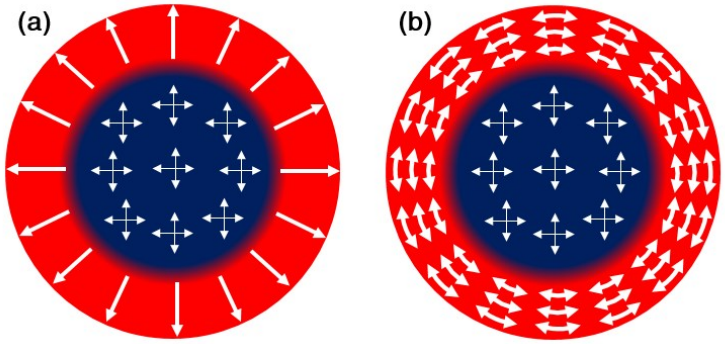

Figure 5. Diffusion and expansion directions for core-shell and homogenous, randomly oriented particle. (a) Diffusion coefficient of a secondary core-shell particle transitioning from homogenous properties (blue) to radial diffusion properties (red). (b) Expansion directions of a core-shell secondary particle transitioning from isotropic expansion (blue) to hoop expansion (red) perpendicular to the diffusion direction.

The general time-dependent diffusion equation for a concentration u solved in this model is given by:

$$\frac{\partial u}{\partial t} + \nabla \cdot (-c\nabla u) = 0 \quad (3)$$

To simulate a full charge followed by discharge, boundary conditions were selected according to experimental charging and discharging profiles found in the literature [9], which indicate that reversible linear charging behaviour is possible in a lithiation state ranging from around 20% to slightly below 100%. For a full charge of the NMC811 particle the initial lithiation state within the particle was set to 100%. A Dirichlet boundary condition prescribing a Li saturation of 20% outside the particle was applied at the particle boundary. The diffusion problem was then solved. In a second step, the diffusion state was linked to a volumetric expansion of the linear-elastic material by prescribing eigenstrain [10,11], assuming a volumetric unit cell contraction of $\Delta V \approx 4\%$ upon full charge [12]. A radial diffusion direction in the shell of core-shell particles was assumed for enhanced lithium diffusion towards the particle centre. The expansion/

contraction direction of the unit cells was therefore prescribed in hoop direction, perpendicular to the diffusion direction (Figure 5b). The core of the core-shell particle was modelled isotropic, resulting in euqi-biaxial expansion without shear strain. The expansion coefficient for a core-shell particle e_{CS} was defined as (4):

$$e_{CS} = \begin{pmatrix} e_x & e_{xy} \\ e_{yx} & e_y \end{pmatrix} = \Delta V \begin{pmatrix} H' + \sin(atan2(y,x))^2 \cdot H & -\cos(atan2(y,x))\sin(atan2(y,x)) \cdot H \\ -\cos(atan2(y,x))\sin(atan2(y,x)) \cdot H & H' + \cos(atan2(y,x))^2 \cdot H \end{pmatrix}$$

With the same H and H' as employed for the diffusion problem. Similarly, the expansion coefficient for a randomly oriented particle e_R was defined as

$$e_R = \begin{pmatrix} e_x & e_{xy} \\ e_{yx} & e_y \end{pmatrix} = \Delta V \begin{pmatrix} 1 & 0 \\ 0 & 1 \end{pmatrix}. \quad (5)$$

Finally, based on the lithiation state u, the strain tensor ε was defined as

$$\varepsilon = \begin{pmatrix} \varepsilon_{11} & \varepsilon_{12} \\ \varepsilon_{21} & \varepsilon_{22} \end{pmatrix} = u \begin{pmatrix} e_x & e_{xy} \\ e_{yx} & e_y \end{pmatrix}, \quad (6)$$

based on which the stress distribution within the particle was caclulated.

The same procedure was followed to determine the strains, stresses and lithium concentration distribution upon discharge, for which the boundary conditions were modified. The lithium saturation within the particle was set to 20%, while the Dirichlet boundary condition was set 100%, simulating lithium diffusion into the particle upon discharge. All simulation results are presented in the following section.

References

[1] T. Li, X.-Z. Yuan, L. Zhang, D. Song, K. Shi, C. Bock, Degradation Mechanisms and Mitigation Strategies of Nickel-Rich NMC-Based Lithium-Ion Batteries, Springer Singapore, 2020. doi:10.1007/s41918-019-00053-3.

[2] J.V. Laveda, J.E. Low, F. Pagani, E. Stilp, S. Dilger, V. Baran, M. Heere, C. Battaglia, Stabilizing Capacity Retention in NMC811/Graphite Full Cells via TMSPi Electrolyte Additives, ACS Appl. Energy Mater. 2 (2019) 7036–7044. doi:10.1021/acsaem.9b00727.

[3] J. Filik, A.W. Ashton, P.C.Y. Chang, P.A. Chater, S.J. Day, M. Drakopoulos, M.W. Gerring, M.L. Hart, O. V. Magdysyuk, S. Michalik, A. Smith, C.C. Tang, N.J. Terrill, M.T. Wharmby, H. Wilhelm, Processing two-dimensional X-ray diffraction and small-angle scattering data in DAWN 2, J. Appl. Crystallogr. 50 (2017) 959–966. doi:10.1107/S1600576717004708.

[4] A.M. Maiden, J.M. Rodenburg, An improved ptychographical phase retrieval algorithm for diffractive imaging, Ultramicroscopy. 109 (2009) 1256–1262. doi:10.1016/j.ultramic.2009.05.012.

[5] H. Sun, K. Zhao, Electronic Structure and Comparative Properties of LiNi x Mn y Co z O 2 Cathode Materials , J. Phys. Chem. C. 121 (2017) 6002–6010. doi:10.1021/acs.jpcc.7b00810.

[6] E.J. Cheng, K. Hong, N.J. Taylor, H. Choe, J. Wolfenstine, J. Sakamoto, Mechanical and physical properties of LiNi0.33Mn0.33Co0.33O2 (NMC), J. Eur. Ceram. Soc. 37 (2017) 3213–3217. doi:10.1016/J.JEURCERAMSOC.2017.03.048.

[7] P.-C. Tsai, B. Wen, M. Wolfman, M.-J. Choe, M.S. Pan, L. Su, K. Thornton, J. Cabana, Y.-M. Chiang, Single-particle measurements of electrochemical kinetics in NMC and NCA cathodes for Li-ion batteries, Energy Environ. Sci. 11 (2018) 860–871. doi:10.1039/C8EE00001H.

[8] E. Zhao, L. Fang, M. Chen, D. Chen, Q. Huang, Z. Hu, Q.B. Yan, M. Wu, X. Xiao, New insight into Li/Ni disorder in layered cathode materials for lithium ion batteries: A joint study of neutron diffraction, electrochemical kinetic analysis and first-principles calculations, J. Mater. Chem. A. 5 (2017) 1679–1686. doi:10.1039/c6ta08448f.

[9] S. Hwang, S.Y. Kim, K.Y. Chung, E.A. Stach, S.M. Kim, W. Chang, Determination of

the mechanism and extent of surface degradation in Ni-based cathode materials after repeated electrochemical cycling, APL Mater. 4 (2016) 096105. doi:10.1063/1.4963723.

[10] E. Salvati, A.M. Korsunsky, A simplified FEM eigenstrain residual stress reconstruction for surface treatments in arbitrary 3D geometries, Int. J. Mech. Sci. 138–139 (2018) 457–466. doi:10.1016/J.IJMECSCI.2018.02.016.

[11] A.M. Korsunsky, A Teaching Essay on Residual Stresses and Eigenstrains, Butterworth-Heinemann, 2017.

[12] Z. Xu, M.M. Rahman, L. Mu, Y. Liu, F. Lin, Chemomechanical behaviors of layered cathode materials in alkali metal ion batteries, J. Mater. Chem. A. 6 (2018) 21859–21884. doi:10.1039/C8TA06875E.